

Supplementary Materials for
Atomic-scale structure of ZrO₂: Formation of metastable polymorphs

Alexandre P. Solomon *et al.*

Corresponding author: Maik K. Lang, mlang2@utk.edu

Sci. Adv. **11**, eadq5943 (2025)
DOI: 10.1126/sciadv.adq5943

This PDF file includes:

Supplementary Text
Figs. S1 to S6
Tables S1 and S2
References

Supplementary Text

Polymorphism in ZrO₂

ZrO₂ is a binary oxide with an atomic structure related to that of fluorite. At standard conditions, bulk ZrO₂ crystals form the monoclinic (m) phase with space group $P2_1/c$ (Fig. S1). At approximately 1400 K, the m-phase transitions to the tetragonal (t) $P4_2/nmc$ phase. Then, at approximately 2600 K the t-phase transitions to the cubic (c) $Fm-3m$ phase (18, 67). Furthermore, near ambient temperatures, the m-phase of ZrO₂ transitions to the high-pressure orthorhombic (hp-o; orthorhombic I) $Pbca$ phase at approximately 4 to 10 GPa (68, 69). All these phases have a center of symmetry and are not polar, thus they do not possess the remnant polarization. The ferroelectricity in ZrO₂ originates from the polar orthorhombic (ferro-o) $Pca2_1$ phase (20). This crystal phase was already reported in 1989 (70), though the electric characterization was not performed then, so that the ferroelectric properties were not unveiled until 2011. There are also other crystal phases, including polar phases, which were theoretically predicted (71). However, these phases have higher energy in comparison to the low energy m, hp-o, ferro-o, and t-phases.

Neutron scattering data and refinements

Spallation neutron diffraction (Fig. S2) supplemented synchrotron X-ray diffraction experiments, and Rietveld analysis of the neutron diffraction patterns (Fig. S3) similarly indicated tetragonal long-range order in both metastable ZrO₂ samples. Pair distribution function (PDF) analysis of neutron total scattering data (Fig. S4) revealed that the short-range order is distinct from any known equilibrium structure and is best described by the $Pbcn$ model.

Figure S5 displays results of a set of preliminary refinements that use a model consisting of an uncorrelated mixture of two phases of tetragonal and orthorhombic symmetry, respectively. In these refinements, the contributions of the two phases are additive, corresponding to a spatially non-uniform uncorrelated binary mixture. The boxcar refinement was performed analyzing a moving r -interval of fixed length. It shows that the PDF signal in the interval is exclusively orthorhombic at short r -values, and it becomes exclusively tetragonal above $r = 20$ Å. Obviously, this result is incompatible with any true physical picture of an uncorrelated binary phase mixture. On the other hand, it clearly supports the image of a collection of nanocrystals made of an assembly of orthorhombic ferroelastic domains. The model also provides a good estimate of the characteristic correlation length of the individual orthorhombic domains ($r = 20$ Å). This value was used to choose a reasonable size of the domains of orthorhombic symmetry and to assemble them in a supercell consisting of all possible ferroelastic orthorhombic variants. This system, built using the broken symmetry elements of the tetragonal long-range symmetry, provides the correct long-range ensemble average that restores the broken tetragonal symmetry at large r -values.

Displacive transformation driven by temperature

The high-temperature polymorph of zirconia is cubic. Lowering temperature below 1300 – 1400 K at ambient pressure produces a tetragonal polymorph. This phase change is usually described by a displacive mechanism involving the zone boundary phonon belonging to the irreducible representation X_2^- (72). This structure is non-polar, described by the space group symmetry

$P4_2/nmc$, and it is characterized by antiparallel shifts of the O atoms along the tetragonal axis direction. The tetragonal lattice is not collinear with the cubic lattice, and the tetragonal orientation is defined by the following lattice transformation of the cubic lattice:

$$[a_T \quad b_T \quad c_T] = [a_C \quad b_C \quad c_C] \begin{bmatrix} 1/2 & -1/2 & 0 \\ 1/2 & 1/2 & 0 \\ 0 & 0 & 1 \end{bmatrix}.$$

Further lowering the temperature leads to another phase transformation to a monoclinic polymorph. The mechanism of this phase transition was described by Negita (32), and it involves the softening of a zone boundary phonon belonging to the M1 irreducible representation of the tetragonal structure, followed immediately by another phonon belonging to the M3 irreducible representation (alternatively, this can be described by a zone center irreducible representation Γ_3^+ in the lattice produced by the condensation of M1). The unstable nature of this phase has been described in terms of an energy landscape with a saddle point shape (coordinates are the amplitudes of the M1 and M3 phonons). A pre-transitional signature of these displacive instabilities was obtained by Rietveld refinement of neutron powder diffraction data of the high-temperature tetragonal polymorph (19). The intermediate unstable phase obtained after the M1 phonon instability has symmetry $Pbcn$, and the relation of this orthorhombic lattice relative to the tetragonal lattice is described by the following transformation matrix followed by a $\mathbf{b}_O/2$ origin shift:

$$[a_O \quad b_O \quad c_O] = [a_T \quad b_T \quad c_T] \begin{bmatrix} -1 & 0 & 1 \\ 1 & 0 & 1 \\ 0 & 1 & 0 \end{bmatrix}.$$

Therefore, the former four-fold axis \mathbf{c}_T now aligns along \mathbf{b}_O . The M1 phonon branch, which couples with strain tensor components of symmetry Γ_4^+ , leads to the differentiation of the orthorhombic a and c axes, affecting the final Zr–O bond lengths. Using a frozen-phonon picture for the phonon branch belonging to this M1 irreducible representation, the structural parameters describing the low-temperature orthorhombic variants can be organized as a superposition of polarization vectors containing the cartesian components of the displacements of each one of the independent atoms. This orthorhombic daughter phase is then a complex medium-range order (MRO) assembly consisting of four $Pbcn$ ferroelastic variants (Fig. 4), providing the mathematical background for the model construction. Each variant is described by a unique combination of symmetry operations, a different superlattice basis, and a specific origin choice.

In bulk samples, the intermediate orthorhombic symmetry is immediately broken by the sudden condensation of the M3 phonon branch that also couples with a shear strain component of symmetry Γ_5^+ , ultimately producing the monoclinic ground state. This instability of symmetry M3 in the tetragonal lattice description, or equivalently Γ_3^+ in the orthorhombic lattice description, brings the system to the monoclinic phase of symmetry $P2_1/c$ (either M3, or equivalently Γ_3^+). This changes the lattice again, aligning the \mathbf{c}_M direction along the former four-fold axis of the tetragonal phase:

$$[a_M \quad b_M \quad c_M] = [a_O \quad b_O \quad c_O] \begin{bmatrix} 0 & 1 & 0 \\ 0 & 0 & 1 \\ 1 & 0 & 0 \end{bmatrix}.$$

Detailed structural parameters of orthorhombic ZrO₂

Neutron PDF fitting parameters of both metastable samples of ZrO₂ (nanocrystalline and ion-irradiated) are provided in Table S1.

EXAFS fitting parameters of metastable, nanocrystalline ZrO₂ are provided in Table S2. Reported uncertainties were output from the structural refinements. Coordination numbers (CNs) were fixed during the fitting. The minimum Debye-Waller factor was limited to $1.0 \times 10^3 \text{ \AA}^2$. The S02 was set to 1.0 for both fittings.

Metastable Pyrochlore

Yb₂Sn₂O₇ pyrochlore was ball-milled for 33 hours, and the transformation to the metastable, defect fluorite phase was observed by X-ray and neutron diffraction using the same procedure as for ZrO₂. A neutron total scattering experiment was performed to probe the SRO of the metastable phase, and the PDF is shown in Figure S6. Neither the pyrochlore (ground-state) nor the defect fluorite (metastable) phase could reproduce the experimental PDF. Rather, the atomic-scale structure of the metastable phase was best described using an orthorhombic, weberite-type (*Cmm*) structural model.

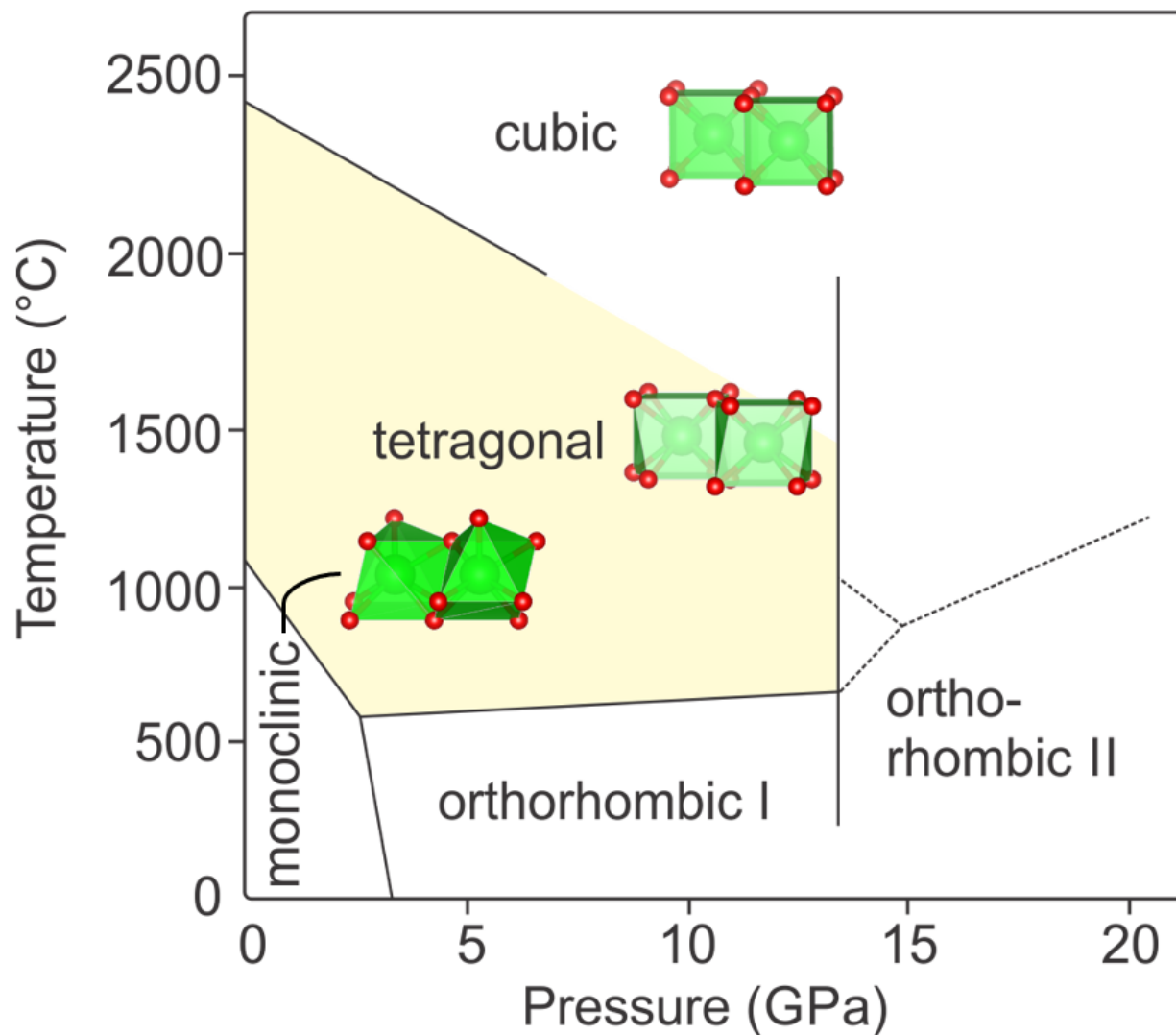


Fig. S1. Phase diagram of ZrO₂ (69). The equilibrium structures accessible at different temperatures are shown with Zr cations in green and oxygen anions in red.

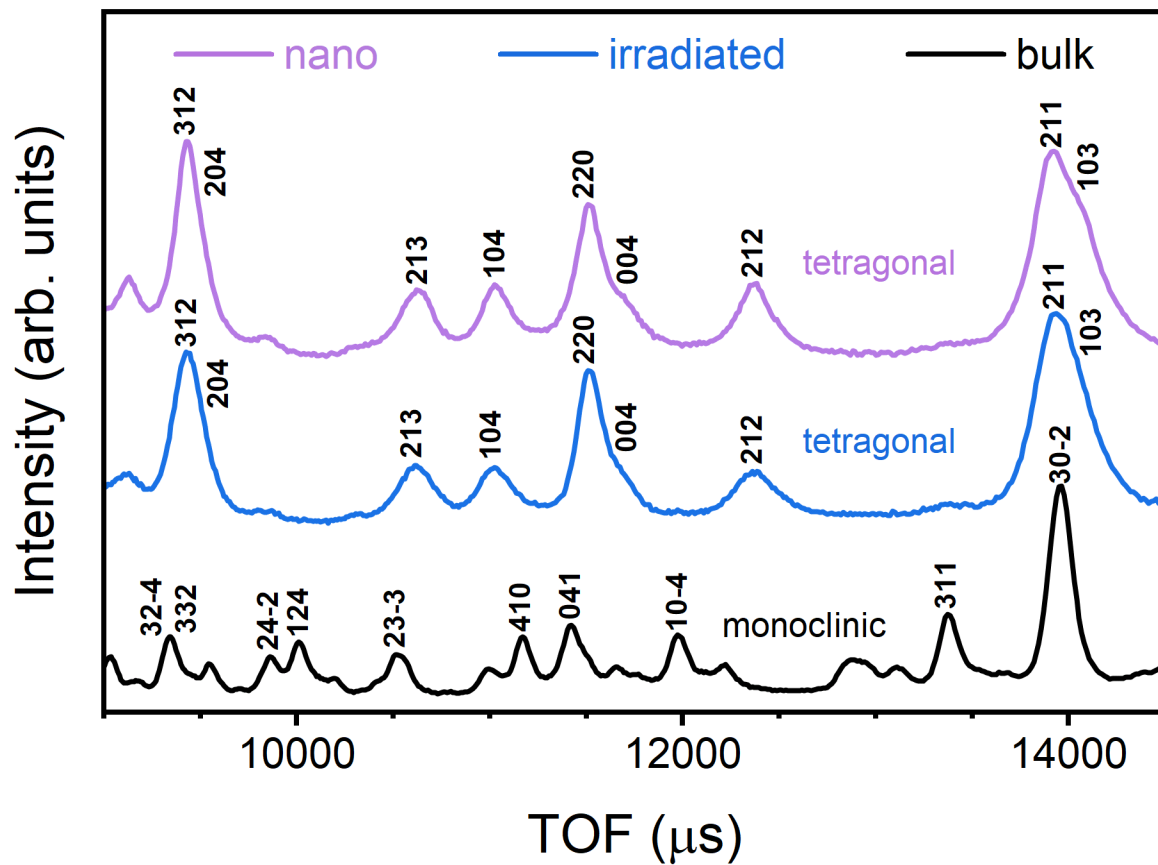


Fig. S2. Neutron diffraction patterns (NOMAD bank 4) shown for bulk, irradiated (1.47 GeV Au, 10^{13} ions cm^{-2}), and nanocrystalline ZrO_2 . Miller indices denote prominent diffraction peaks. All peaks are indexed by the monoclinic and tetragonal phases. The diffraction patterns are offset vertically for ease of visualization.

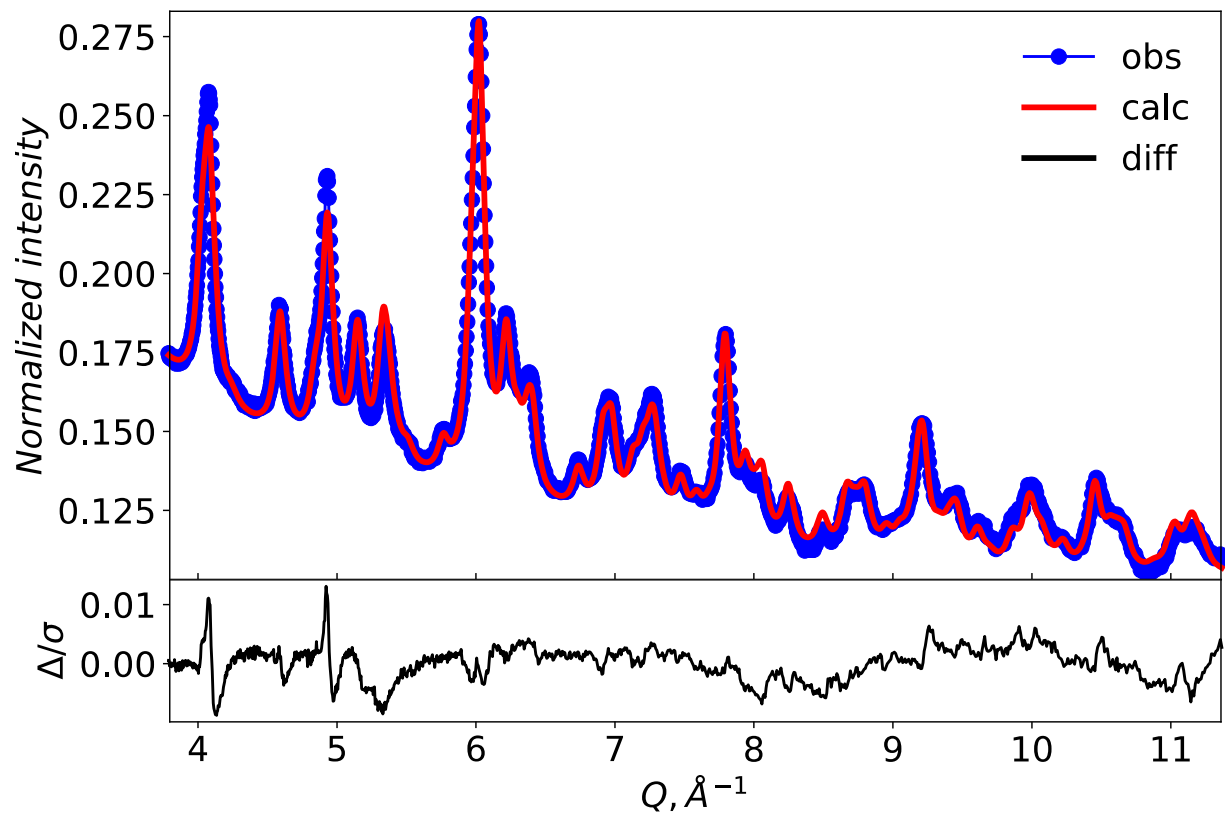


Fig. S3. Representative Rietveld refinement of neutron diffraction pattern for nanocrystalline ZrO_2 . The refinement was performed using the high temperature tetragonal phase polymorph and data collected using bank 4 of the NOMAD instrument. Blue circles represent experimental data, the red curve was calculated from the refined structure, and the difference curve is given in black.

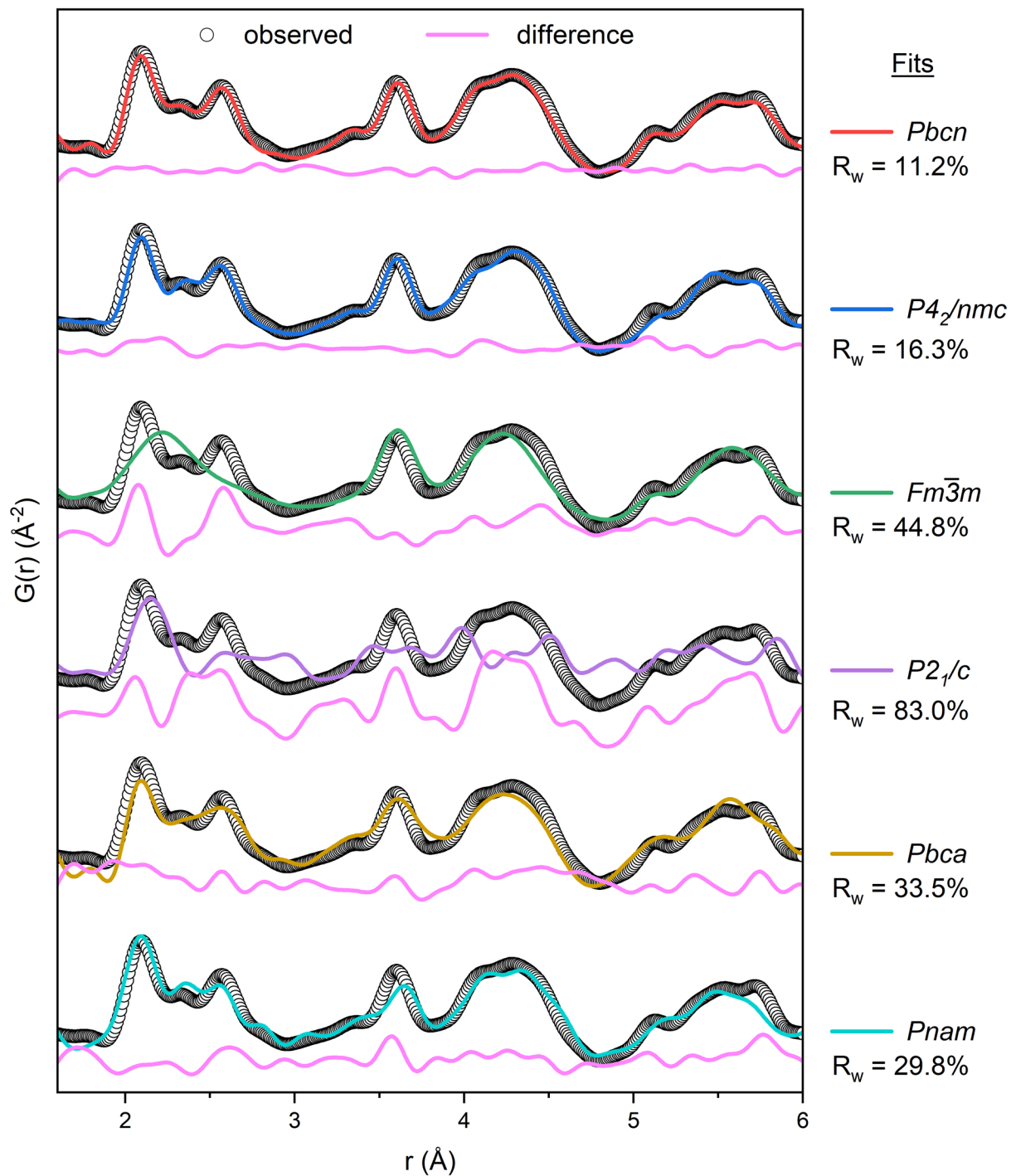


Fig. S4. Fits of known structures to experimental PDF. Calculated fits (colored lines) from small-box refinements of known ZrO_2 structures refined over $1.6 \leq r \leq 6.0 \text{ Å}$ are compared to the experimental PDF (open black circles) of nanocrystalline ZrO_2 . The absolutely scaled PDFs are each offset by a constant amount along the y-axis. Respective difference curves are shown in magenta, and weighted residuals are reported as R_w .

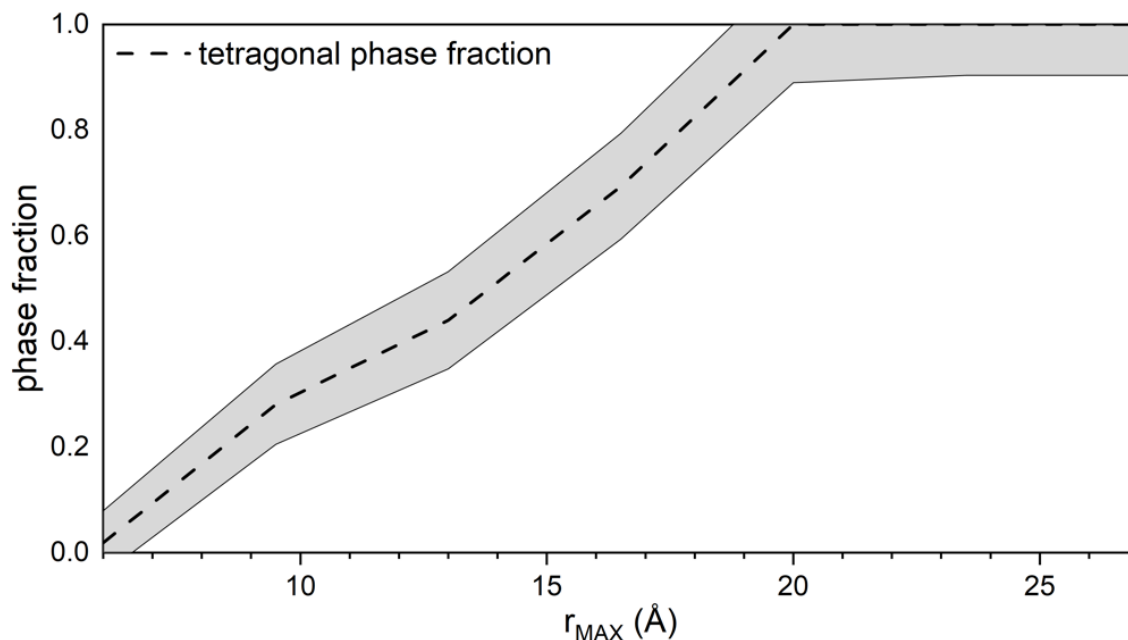


Fig. S5. Phase fractions determined from two-phase boxcar refinements of the nanocrystalline ZrO_2 neutron PDF. Tetragonal and orthorhombic phase fractions exhibit a dependence on the real space range sampled. No tetragonal pair correlations are observed at r -values below $\sim 6\text{--}7$ Å, and little to no intensity from orthorhombic pair correlations is observed above ~ 20 Å. Each boxcar spans 4.2 Å (e.g., $1.8 \leq r \leq 6.0$ Å). Phase fractions shown are the mass fractions calculated by PDFgui.

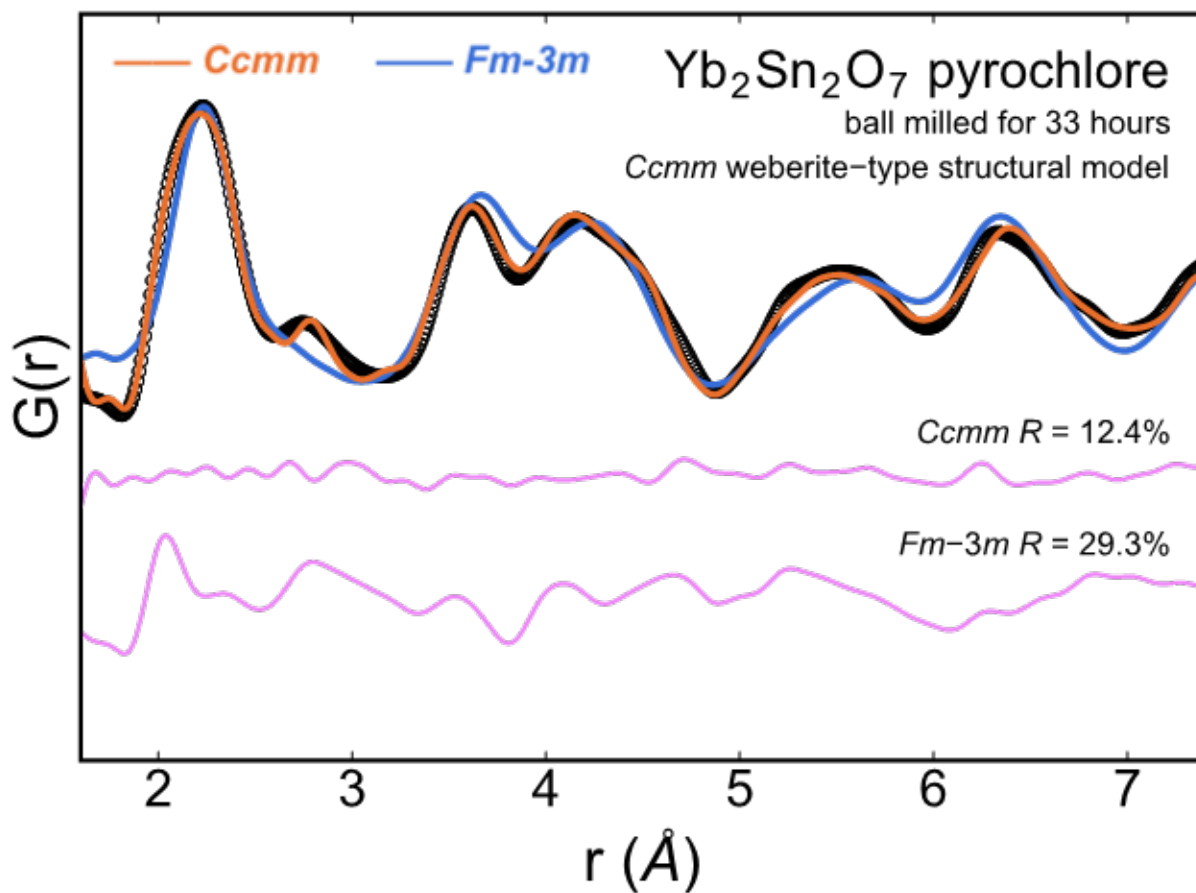


Fig. S6. Neutron pair distribution function of mechanically milled $\text{Yb}_2\text{Sn}_2\text{O}_7$. Fits to the cubic, defect fluorite ($Fm-3m$) and orthorhombic, weberite-type ($Ccmm$) models are shown in orange and blue, respectively. Magenta curves show the difference between the data (black circles) and the models (colored lines), and weighted residuals are reported as R .

	x	y	z	$U_{\text{iso}} (\text{\AA}^2)$	a (\AA)	b (\AA)	c (\AA)
<i>Nanocrystalline</i>							
Zr1	0	0.744(4)	0.25	0.005(1)			
O1	0.733(4)	0.045(2)	0.988(3)	0.012(5)	5.04(2)	5.18(2)	5.13(2)
<i>Irradiated</i>							
Zr1	0	0.742(3)	0.25	0.005(1)			
O1	0.734(4)	0.045(2)	0.988(2)	0.013(5)	5.05(2)	5.18(2)	5.13(2)

Table S1. Neutron PDF fitting parameters of metastable ZrO_2 samples with *Pbcn* structure. Uncertainties shown represent one standard deviation.

<i>Pbcn</i>					
Path	CN	R (Å)	Sigma ($\times 10^4 \text{ \AA}^2$)	ΔE (eV)	Theor. R (Å)
Zr-O1a	2.0	2.09(1)	10(1)		2.06
Zr-O1b	2.0	2.09(1)	10(1)		2.13
Zr-O1c	2.0	2.20(1)	10(7)		2.27
Zr-O1d	2.0	2.29(1)	10(8)		2.45
Zr-O1-O1a	4.0	3.35(37)	10(1)		3.39
Zr-O1-O1b*	4.0	3.48	10.		3.46
Zr-O1-O1c*	4.0	3.51	10.	-4.0(5)	3.50
Z-O1-O1d*	4.0	3.53	10.		3.56
Zr-Zr1a	2.0	3.58(1)	29(6)		3.58
Zr-Zr1b	4.0	3.69(1)	21(2)		3.60
Zr-Zr1c	4.0	3.50(1)	64(6)		3.63
Zr-Zr1d	2.0	3.61(1)	32(6)		3.71
Zr-O2a	2.0	4.32(8)	10(30)		4.07
Zr-O2b	2.0	4.24(5)	11(60)		4.08
<i>P4₂/nmc</i>					
Zr-O1a	4.0	2.10(1)	10(6)		2.09
Zr-O1b	4.0	2.28(1)	46(12)		2.36
Zr-Zr1a	4.0	3.52(1)	13(29)	2.9(7)	3.60
Zr-Zr1b	4.0	3.71(1)	14(3)		3.63
Zr-Zr1c	4.0	3.62(1)	10(3)		3.64

*Fixed parameters

Table S2. EXAFS fitting parameters of nanocrystalline ZrO₂ sample with *Pbcn* and *P4₂/nmc* structures.

REFERENCES AND NOTES

1. C. Suryanarayana, Mechanical alloying and milling. *Prog. Mater. Sci.* **46**, 1–184 (2001).
2. D. B. Miracle, O. N. Senkov, A critical review of high entropy alloys and related concepts. *Acta Mater.* **122**, 448–511 (2017).
3. W. Mao, Y. Lin, Making the most of metastability. *Science* **377**, 814–815 (2022).
4. Z. M. Li, K. G. Pradeep, Y. Deng, D. Raabe, C. C. Tasan, Metastable high-entropy dual-phase alloys overcome the strength-ductility trade-off. *Nature* **534**, 227–230 (2016).
5. J. Lian, L. Wang, J. Chen, K. Sun, R. C. Ewing, J. M. Farmer, L. A. Boatner, The order-disorder transition in ion-irradiated pyrochlore. *Acta Mater.* **51**, 1493–1502 (2003).
6. A. A. Balandin, Thermal properties of graphene and nanostructured carbon materials. *Nat. Mater.* **10**, 569–581 (2011).
7. H. Tang, K. Prasad, R. Sanjines, P. E. Schmid, F. Levy, Electrical and optical-properties of TiO₂ anatase thin-films. *J. Appl. Phys.* **75**, 2042–2047 (1994).
8. D. Simeone, G. Baldinozzi, D. Gosset, S. LeCaer, L. Mazerolles, Impact of radiation defects on the structural stability of pure zirconia. *Phys. Rev. B* **70**, 134116 (2004).
9. L. M. Acuna, D. G. Lamas, R. O. Fuentes, I. O. Fabregas, M. C. A. Fantini, A. F. Craievich, R. J. Prado, Local atomic structure in tetragonal pure ZrO₂ nanopowders. *J. Appl. Cryst.* **43**, 227–236 (2010).
10. N. Nakamura, L. S. Su, H. Wang, N. Bernstein, S. K. Jha, E. Culbertson, H. Y. Wang, S. J. L. Billinge, C. S. Hellberg, B. Reeja-Jayan, Linking far-from-equilibrium defect structures in ceramics to electromagnetic driving forces. *J. Mater. Chem. A* **9**, 8425–8434 (2021).
11. A. C. Dippel, M. Roelsgaard, U. Boettger, T. Schneller, O. Gutowski, U. Ruett, Local atomic structure of thin and ultrathin films via rapid high-energy X-ray total scattering at grazing incidence. *IUCrJ* **6**, 290–298 (2019).

12. T. Y. Xiao, Y. Nagaoka, X. R. Wang, T. Jiang, D. LaMontagne, Q. Zhang, C. Cao, X. Z. Diao, J. H. Qiu, Y. R. Lu, Z. W. Wang, Y. C. Cao, Nanocrystals with metastable high-pressure phases under ambient conditions. *Science* **377**, 870–874 (2022).
13. M. Gateshki, V. Petkov, G. Williams, S. K. Pradhan, Y. Ren, Atomic-scale structure of nanocrystalline ZrO₂ prepared by high-energy ball milling. *Phys. Rev. B* **71**, 224107 (2005).
14. S. Shukla, S. Seal, Mechanisms of room temperature metastable tetragonal phase stabilisation in zirconia. *Int. Mater. Rev.* **50**, 45–64 (2005).
15. A. P. Solomon, C. L. Tracy, E. C. O'Quinn, D. Severin, M. K. Lang, Transformations to amorphous and X-type phases in swift heavy ion-irradiated Ln₂O₃ and Mn₂O₃. *J. Appl. Phys.* **129**, 225903 (2021).
16. B. Schuster, F. Fujara, B. Merk, R. Neumann, T. Seidl, C. Trautmann, Response behavior of ZrO₂ under swift heavy ion irradiation with and without external pressure. *Nucl. Instrum. Methods Phys. Res. B* **277**, 45–52 (2012).
17. G. Fadda, G. Zanzotto, L. Colombo, First-principles study of the effect of pressure on the five zirconia polymorphs. I. Structural, vibrational, and thermoelastic properties. *Phys. Rev. B* **82**, 064105 (2010).
18. J. Chevalier, L. Gremillard, A. V. Virkar, D. R. Clarke, The tetragonal-monoclinic transformation in zirconia: Lessons Learned and future trends. *J. Am. Ceram. Soc.* **92**, 1901–1920 (2009).
19. D. Simeone, G. Baldinozzi, D. Gosset, M. Dutheil, A. Bulou, T. Hansen, Monoclinic to tetragonal semireconstructive phase transition of zirconia. *Phys. Rev. B* **67**, 064111 (2003).
20. J. Muller, T. S. Boscke, U. Schroder, S. Mueller, D. Brauhaus, U. Bottger, L. Frey, T. Mikolajick, Ferroelectricity in simple binary ZrO₂ and HfO₂. *Nano Lett.* **12**, 4318–4323 (2012).
21. J. W. Christian, G. B. Olson, M. Cohen, Classification of displacive transformations: What is a martensitic transformation? *J. Phys. IV* **5**, 3–10 (1995).

22. Y. Zhang, H. X. Chen, L. Duan, J. B. Fan, L. Ni, V. Ji, A comparison study of the structural and mechanical properties of cubic, tetragonal, monoclinic, and three orthorhombic phases of ZrO₂. *J. Alloys Compd.* **749**, 283–292 (2018).
23. R. C. Garvie, Occurrence of metastable tetragonal zirconia as a crystallite size effect. *J. Phys. Chem.* **69**, 1238–1243 (1965).
24. M. Lang, F. X. Zhang, J. M. Zhang, J. W. Wang, J. Lian, W. J. Weber, B. Schuster, C. Trautmann, R. Neumann, R. C. Ewing, Review of A₂B₂O₇ pyrochlore response to irradiation and pressure. *Nucl. Instrum. Methods Phys. Res. B* **268**, 2951–2959 (2010).
25. K. E. Sickafus, H. Matzke, T. Hartmann, K. Yasuda, J. A. Valdez, P. Chodak, M. Nastasi, R. A. Verrall, Radiation damage effects in zirconia. *J. Nucl. Mater.* **274**, 66–77 (1999).
26. A. Benyagoub, Mechanism of the monoclinic-to-tetragonal phase transition induced in zirconia and hafnia by swift heavy ions. *Phys. Rev. B* **72**, 094114 (2005).
27. G. K. Williamson, W. H. Hall, X-ray line broadening from filed aluminium and wolfram. *Acta Metall.* **1**, 22–31 (1953).
28. D. A. Keen, A. L. Goodwin, The crystallography of correlated disorder. *Nature* **521**, 303–309 (2015).
29. B. Bondars, G. Heidemane, J. Grabis, K. Laschke, H. Boysen, J. Schneider, F. Frey, Powder diffraction investigations of plasma sprayed zirconia. *J. Mater. Sci.* **30**, 1621–1625 (1995).
30. M. Dapiaggi, F. Maglia, L. Pagliari, I. G. Tredici, N. Rotiroti, The role of local structural distortions in the stabilisation of undoped nanocrystalline tetragonal zirconia. *Mater. Chem. Phys.* **147**, 395–402 (2014).
31. W. Cochran, Crystal stability and the theory of ferroelectricity. *Phys. Rev. Lett.* **9**, 387–423 (1960).

32. K. Negita, H. Takao, Condensations of phonons at the tetragonal to monoclinic phase-transition in ZrO_2 . *J. Phys. Chem. Solid* **50**, 325–331 (1989).
33. P. A. Lee, P. H. Citrin, P. Eisenberger, B. M. Kincaid, Extended x-ray absorption fine-structure—Its strengths and limitations as a structural tool. *Rev. Mod. Phys.* **53**, 769–806 (1981).
34. C. Boulesteix, M. Bensalem, B. Yanguì, Domain-structures and plasticity of ferroelastic materials: Case of rare-earth sesquioxides and $\text{YBa}_2\text{Cu}_3\text{O}_7$. *J. Less Common Met.* **156**, 29–41 (1989).
35. E. K. H. Salje, Ferroelastic domain walls as templates for multiferroic devices. *J. Appl. Phys.* **128**, 164104 (2020).
36. K. Dörr, Ferroelastic domains springy expansion. *Nat. Mater.* **15**, 497–498 (2016).
37. B. H. Toby, R. B. Von Dreele, GSAS-II: The genesis of a modern open-source all purpose crystallography software package. *J. Appl. Cryst.* **46**, 544–549 (2013).
38. R. B. Neder, F. Frey, H. Schulz, Diffraction theory for diffuse-scattering by correlated microdomains in materials with several atoms per unit-cell. *Acta Crystallogr. A* **46**, 792–798 (1990).
39. K. P. McKenna, F. Hofer, D. Gilks, V. K. Lazarov, C. L. Chen, Z. C. Wang, Y. Ikuhara, Atomic-scale structure and properties of highly stable antiphase boundary defects in Fe_3O_4 . *Nat. Commun.* **5**, 5740 (2014).
40. E. K. H. Salje, Application of Landau theory for the analysis of phase transitions in minerals. *Phys. Rep.* **215**, 49–99 (1992).
41. G. Baldinozzi, D. Simeone, D. Gosset, M. Dutheil, Neutron diffraction study of the size-induced tetragonal to monoclinic phase transition in zirconia nanocrystals. *Phys. Rev. Lett.* **90**, 216103 (2003).

42. E. C. O'Quinn, K. E. Sickafus, R. C. Ewing, G. Baldinozzi, J. C. Neuefeind, M. G. Tucker, A. F. Fuentes, D. Drey, M. K. Lang, Predicting short-range order and correlated phenomena in disordered crystalline materials. *Sci. Adv.* **6**, eabc2758 (2020).
43. J. Shamblin, M. Feyngenson, J. Neuefeind, C. L. Tracy, F. X. Zhang, S. Finkeldei, D. Bosbach, H. D. Zhou, R. C. Ewing, M. Lang, Probing disorder in isometric pyrochlore and related complex oxides. *Nat. Mater.* **15**, 507–511 (2016).
44. J. Shamblin, C. L. Tracy, R. I. Palomares, E. C. O'Quinn, R. C. Ewing, J. Neuefeind, M. Feyngenson, J. Behrens, C. Trautmann, M. Lang, Similar local order in disordered fluorite and aperiodic pyrochlore structures. *Acta Mater.* **144**, 60–67 (2018).
45. E. C. O'Quinn, C. L. Tracy, W. F. Cureton, R. Sachan, J. C. Neuefeind, C. Trautmann, M. K. Lang, Multi-scale investigation of heterogeneous swift heavy ion tracks in stannate pyrochlore. *J. Mater. Chem. A* **9**, 16982–16997 (2021).
46. C. K. Chung, E. C. O'Quinn, J. C. Neuefeind, A. F. Fuentes, H. W. Xu, M. Lang, A. Navrotsky, Thermodynamic and structural evolution of mechanically milled and swift heavy ion irradiated $\text{Er}_2\text{Ti}_2\text{O}_7$ pyrochlore. *Acta Mater.* **181**, 309–317 (2019).
47. K. E. Sickafus, L. Minervini, R. W. Grimes, J. A. Valdez, M. Ishimaru, F. Li, K. J. McClellan, T. Hartmann, Radiation tolerance of complex oxides. *Science* **289**, 748–751 (2000).
48. P. F. McMillan, New materials from high-pressure experiments. *Nat. Mater.* **1**, 19–25 (2002).
49. C. Yang, K. Trachenko, S. Hull, I. T. Todorov, M. T. Dove, Emergence of microstructure and oxygen diffusion in yttrium-stabilized cubic zirconia. *Phys. Rev. B* **97**, 184107 (2018).
50. M. Fèvre, A. Finel, R. Caudron, Local order and thermal conductivity in yttria-stabilized zirconia. I. Microstructural investigations using neutron diffuse scattering and atomic-scale simulations. *Phys. Rev. B* **72**, 104117 (2005).

51. K. P. Kelley, A. N. Morozovska, E. A. Eliseev, Y. T. Liu, S. S. Fields, S. T. Jaszewski, T. Mimura, S. Calderon, E. C. Dickey, J. F. Ihlefeld, S. V. Kalinin, Ferroelectricity in hafnia controlled via surface electrochemical state. *Nat. Mater.*, **22**, 1144–1151 (2023).
52. S. Petzold, S. U. Sharath, J. Lemke, E. Hildebrandt, C. Trautmann, L. Alff, Heavy ion radiation effects on hafnium oxide-based resistive random access memory. *IEEE Trans. Nucl. Sci.* **66**, 1715–1718 (2019).
53. M. Lederer, T. Vogel, T. Kämpfe, N. Kaiser, E. Piros, R. Olivo, T. Ali, S. Petzold, D. Lehninger, C. Trautmann, L. Alff, K. Seidel, Heavy ion irradiation induced phase transitions and their impact on the switching behavior of ferroelectric hafnia. *J. Appl. Phys.* **132**, 064102 (2022).
54. A. Parija, G. R. Waetzig, J. L. Andrews, S. Banerjee, traversing energy landscapes away from equilibrium: Strategies for accessing and utilizing metastable phase space. *J. Phys. Chem. C* **122**, 25709–25728 (2018).
55. R. Thomas, J. F. Scott, D. N. Bose, R. S. Katiyar, Multiferroic thin-film integration onto semiconductor devices. *J. Phys. Condens. Matter* **22**, 423201 (2010).
56. B. J. Campbell, H. T. Stokes, D. E. Tanner, D. M. Hatch, ISODISPLACE: A web-based tool for exploring structural distortions. *J. Appl. Cryst.* **39**, 607–614 (2006).
57. A. P. Drozdov, M. I. Erements, I. A. Troyan, V. Ksenofontov, S. I. Shylin, Conventional superconductivity at 203 kelvin at high pressures in the sulfur hydride system. *Nature* **525**, 73–76 (2015).
58. L. J. Zhang, Y. C. Wang, J. Lv, Y. M. Ma, Materials discovery at high pressures. *Nat. Rev. Mater.* **2**, 17005 (2017).
59. H. M. Rietveld, A profile refinement method for nuclear and magnetic structures. *J. Appl. Cryst.* **2**, 65–71 (1969).
60. J. F. Ziegler, M. D. Ziegler, J. P. Biersack, SRIM—The stopping and range of ions in matter (2010). *Nucl. Instrum. Methods Phys. Res. B* **268**, 1818–1823 (2010).

61. R. I. Palomares, J. Shamblin, C. L. Tracy, J. Neufeind, R. C. Ewing, C. Trautmann, M. Lang, Defect accumulation in swift heavy ion-irradiated CeO₂ and ThO₂. *J. Mater. Chem. A* **5**, 12193–12201 (2017).
62. X. B. Shi, S. Ghose, E. Dooryhee, Performance calculations of the X-ray powder diffraction beamline at NSLS-II. *J. Synchrot. Radiat.* **20**, 234–242 (2013).
63. J. D. Beal, K. D. Berry, R. A. Riedel, L. L. Funk, W. B. Reynolds, Y. Diawara, The NOMAD instrument neutron detector array at the SNS. *Nucl. Instrum. Methods Phys. Res. A* **1018**, 165851 (2021).
64. C. L. Farrow, P. Juhas, J. W. Liu, D. Bryndin, E. S. Bozin, J. Bloch, T. Proffen, S. J. L. Billinge, PDFfit2 and PDFgui: Computer programs for studying nanostructure in crystals. *J. Phys. Condens. Matter* **19**, 335219 (2007).
65. M. Lang, C. L. Tracy, R. I. Palomares, F. X. Zhang, D. Severin, M. Bender, C. Trautmann, C. Park, V. B. Prakapenka, V. A. Skuratov, R. C. Ewing, Characterization of ion-induced radiation effects in nuclear materials using synchrotron x-ray techniques. *J. Mater. Res.* **30**, 1366–1379 (2015).
66. B. Ravel, M. Newville, Athena, Artemis, Hephaestus: Data analysis for X-ray absorption spectroscopy using IFEFFIT. *J. Synchrot. Radiat.* **12**, 537–541 (2005).
67. R. Ruh, H. J. Garrett, R. F. Domagala, N. M. Tallan, System zirconia-hafnia. *J. Am. Ceram. Soc.* **51**, 23–28 (1968).
68. Y. Al-Khatatbeh, K. K. M. Lee, B. Kiefer, Phase relations and hardness trends of ZrO₂ phases at high pressure. *Phys. Rev. B* **81**, 214102 (2010).
69. B. Schuster, M. Lang, R. Klein, C. Trautmann, R. Neumann, A. Benyagoub, Structural phase transition in ZrO₂ induced by swift heavy ion irradiation at high-pressure. *Nucl. Instrum. Methods Phys. Res. B* **267**, 964–968 (2009).

70. E. H. Kisi, C. J. Howard, R. J. Hill, Crystal-structure of orthorhombic zirconia in partially stabilized zirconia. *J. Am. Ceram. Soc.* **72**, 1757–1760 (1989).
71. S. E. Reyes-Lillo, K. F. Garrity, K. M. Rabe, Antiferroelectricity in thin-film ZrO₂ from first principles. *Phys. Rev. B* **90**, 140103 (2014).
72. G. M. Rignanese, F. Detraux, X. Gonze, A. Pasquarello, First-principles study of dynamical and dielectric properties of tetragonal zirconia. *Phys. Rev. B* **64**, 134301 (2001).